Journal of Materials Chemistry A

PAPER

View Article Online
View Journal | View Issue

Cite this: J. Mater. Chem. A, 2014, 2, 11134

Low temperature sintering of binder-containing TiO_2/metal peroxide pastes for dye-sensitized solar cells†

Peter J. Holliman,*[ab] Dhiyaa K. Muslem,[a] Eurig W. Jones,[a] Arthur Connell,[a] Matthew L. Davies,[a] Cecile Charbonneau,[b] Matthew J. Carnie[b] and David A. Worsley[b]

Received 27th February 2014
Accepted 2nd May 2014

DOI: 10.1039/c4ta01000k

www.rsc.org/MaterialsA

Nano-structured metal oxide films are key components of dye-sensitized (DSC) solar cells. Scaling such devices requires lower temperature processing to enable cheaper substrates to be used. In this context, we report a new and scalable method to sinter binder-containing metal oxide pastes to make DSC photo-electrodes at lower temperatures. Metal peroxide powders (CaO_2, MgO_2, or ZnO_2) were added to terpineol-based P25 pastes containing ethyl cellulose binder or to commercial TiO_2 paste (DSL18NR-T). Thermal analysis shows that binder decomposition occurs at 300 °C instead of the standard 450 °C for a TiO_2-only paste and suggests that the metal peroxides act as combustion promoters releasing heat and oxygen within the film while heating. The data show that this heat and oxygen release coincide best with binder combustion for ZnO_2 and DSC device tests show that adding ZnO_2 to TiO_2 pastes produces the best performances affording $\eta = 7.5\%$ for small devices (0.26 cm^2) and $\eta = 5.7\%$ at 300 °C or 450 °C for DSL18NR-T/ZnO_2 for larger (1 cm^2) devices. To the best of our knowledge, the performance of the (0.26 cm^2) cells is comparable to the highest efficiency devices reported for DSCs fabricated using low temperature methods. The device efficiency is most strongly linked with J_{sc}; BET and dye sorption measurements suggest that J_{sc} is linked with the metal oxide surface area and dye loading. The latter is linked to the availability of surface sorption sites for dye molecules which is strongly negatively affected by any residual organic binder which resulted from incomplete combustion.

O'Regan and Grätzel's breakthrough in dye-sensitised solar cell (DSC) technology[1] showed that sintering pre-made TiO_2 nanocrystals[2–4] at 450–600 °C significantly increases the photo-anode surface area, dye loading and short circuit current. This has led to considerable interest in DSC devices as promising candidates for large scale, low cost PVs because they should be manufacturable using printing and roll-to-roll processing using abundant and non-toxic raw materials.[5,6]

For DSC devices, the mechanical and electrical connectivity between the TiO_2 particles are key to long-term device function as charge must travel through the photo-electrode to the current collecting working electrode.[7] Typically this is achieved by printing a colloidal suspension of well-dispersed, crystalline TiO_2 nanoparticles where the paste rheology is controlled by the addition of a long-chain organic polymer (the binder). The binder enables crack-free films to be printed with variable but controlled film thicknesses at a range of length scales. Without the binder, it is impossible to print large enough photo-electrodes to scale the technology. This means that currently printed films must be sintered at >450 °C to completely combust the organic binder to free up dye sorption sites on the surface of the TiO_2 particles and to enable the formation of robust inter-particle connections but low enough to minimise any reduction in the TiO_2 surface area. However, this limits the working electrode substrate to FTO-coated glass or Ti foil[8] which are inflexible and heavy or expensive,[9] respectively. By comparison, cheaper, more lightweight and flexible substrates which are suitable for large-scale roll-to-roll manufacture (*e.g.* metal foils, TCO-coated plastic) require lower processing temperatures; typically 300 °C for metal foils and 150 °C for plastics.[10] However, there are no reports in the literature to date of methods of sintering binder-containing pastes at low temperature.

Instead, although low temperature sintering of photo-anodes for DSCs has been widely studied, reports have centred on using binder-free pastes. However, as discussed previously, binder-free pastes are significantly limited for larger scale applications because of the difficulties in controlling printability and film consistency over wider areas (*e.g.* film thickness, and inter-particle adhesion which can lead to cracking and

[a]School of Chemistry, Bangor University, Gwynedd LL57 2UW, UK. E-mail: p.j.holliman@bangor.ac.uk; Fax: +44 (0)1248 370528; Tel: +44 (0)1248 382375
[b]SPECIFIC, College of Engineering Swansea University, Baglan Bay Innovation and Knowledge Centre, Port Talbot SA12 7AZ, UK

† Electronic supplementary information (ESI) available. See DOI: 10.1039/c4ta01000k

substrate adhesion which can lead to delamination). Binder-free approaches include spin coating,[11] sol gel,[12] hydrothermal treatment[13–15] chemical sintering,[16,17] pressure sintering,[18–20] electrophoretic deposition of TiO_2 nanoparticles,[21] varying TiO_2 particles[22] and the use of electron beam showers.[23] Variations in radiant heating have also been studied including laser treatment,[24] microwave irradiation[25] and post-sintering O_2 plasma[26] aimed at removing residual organic matter from the metal oxide surface. Whilst these approaches have shown promise at the laboratory scale, producing consistent, large-scale meso-porous films for DSC device manufacturing will require the presence of a binder in the TiO_2 colloid. Hence, the study of low temperature approaches to sintering binder-containing metal oxide pastes remains a key challenge for DSC manufacturing.

In this context, this paper reports a new approach to lower sintering temperatures of binder-containing metal oxide pastes to manufacture photo-electrodes for DSCs. We believe this is the first report using solid peroxides as combustion promoters. This approach enables accurate control of paste rheology by retaining an organic polymer binder in the metal oxide pastes which is essential to produce coherent, large scale films with consistent thickness. Our combined experimental approach is to screen larger films (3 × 2 cm) to examine film coherence and colour, to understand the fundamental thermal chemistry of screen printing pastes and how this influences sintering and then to make larger DSC devices than are typically reported (1 cm^2) to test the effects of sintering on performance. Finally, we have studied the metal oxide area and dye loading to investigate the links between the short circuit current and sintering treatment.

Experimental

Paste and device manufacture

P25 pastes were prepared by thoroughly mixing P25 (16 g, Degussa) with terpineol (64.9 g, Fluka) and ethyl cellulose (8 g, Fluka Product# 46070). Peroxide containing pastes were prepared by adding calcium peroxide, magnesium peroxide or zinc peroxide (10% w/w *versus* TiO_2, all Aldrich) and thoroughly mixing for 1 h. Commercial DSL18NR-T paste (Dyesol) was either used as purchased and metal peroxides were added as described above.

Photo-electrodes were prepared by doctor blading the metal oxide paste onto FTO-coated glass (TEC15, NSG) and sintering in air at either 450 °C, 300 °C or 150 °C for 30 min. Larger films were prepared (3 × 2 cm) to study film coherence over a larger area. DSC devices were prepared using 1 cm^2 films (minimum 3 replicates per treatment) to study film coherence and reproducibility. Selected films were then immersed in 40 mM $TiCl_4$–$THF_{2(aq)}$ at 70 °C for 30 min before rinsing with water and air drying for 10 min. The films were then re-sintered at the same temperature used during the first sintering process so that no film experienced a temperature greater than its initial sintering temperature at any point during processing.

Counter electrodes were prepared by spreading the PT1 paste (Dyesol) onto TEC 8 glass (NSG) and heating to 400 °C in air for 30 min. The photo and counter electrodes were then sealed together using a Surlyn gasket at 120 °C followed by fast dyeing with 0.3 mM N719 (Dyesol) in acetonitrile–*tert*-butanol (1 : 1 v/v) for 10 min as described previously.[27] The electrolyte was 0.8 M 1-methyl-3-propyl imidazolium iodide, 0.05 M *tert*-butyl ammonium iodide, 0.05 M I_2, 0.3 M benzimidazole and 0.05 M guanidinium thiocyanate in acetonitrile.

Device characterization

Current–voltage characteristics were studied using an ABET Solar Simulator with a Xe arc lamp and a Keithley 2400 at 100 mW cm^{-2} or 1 Sun between 0 and 1 V. The spectral response was measured from 300–800 nm on a QE×10 Quantum Efficiency Measurement System in DC mode at a resolution of 10 nm. Lamps were calibrated to 1 Sun (100 mW cm^{-2}) using a certified (Oriel 91150V) mono-crystalline Si reference cell traceable to the National Renewable Energy Laboratory (NREL).

Photocurrent and photovoltage transients were measured as described in ref. 28. The white bias light was provided by a BRIDGELUX 9000 lumen LED array (Farnell) whilst the pulse light was provided by a bank of four OSLON PowerCluster green LED arrays (RS). The pulse intensity was chosen to make sure $\Delta V < 10$ mV above V_{OC}. A pulse length of 250 μs was utilized and was generated *via* a fast MOSFET transistor controlled by a National Instruments USB-6251 data acquisition board (DAQ) and WaveMetrics IGOR Pro software. Voltages were measured directly using the DAQ whilst currents were measured *via* a voltage drop against a 1 Ω resistor.

XRD was carried out using a PANalytical diffractometer at 45 kV and 35 mA between 20 and 60° 2θ using Ni-filtered Cu-$K_{\alpha 1}$ radiation (λ = 1.5405°A). Thermal gravimetric analysis and differential scanning calorimetry were performed using a SDTQ600 TGA/DSC (TA Instruments Ltd). The pastes were either run as prepared or were pre-dried at 100–110 °C for 2 h to evaporate the solvent to focus the analysis on binder combustion. The samples were ramped at 10 °C min^{-1} between room temperature and 600 °C under flowing air. The surface area of pre-sintered doctor-bladed films was determined using BET (Brunauer–Emmett–Teller) isotherms at −196 °C using a Micromeritics Gemini III 2375. Electron microscopy and energy dispersive X-ray elemental analyses were performed on a Field Emission Gun-Scanning Electron Microscope (FEG-SEM) Hitachi S-4800 (12 keV, 10 μA) equipped with an Oxford instruments X-Max (50 mm^2 window) detector.

N719 dye sorption was studied using sintered P25 and P25/ZnO_2 films either by directly immersing the film in N719 dye solution for 24 h or by scraping sintered films off a glass substrate and immersing the collected powder into N719 dye solution for 24 h. N719 uptake was quantified by first desorbing the dye using 0.1 M $NaOH_{(aq)}$–ethanol (1 : 1 v/v) followed by calculation of the concentration of the desorbed solution using UV-visible spectroscopy at 512 nm in conjunction with a calibration graph (see ESI Fig. 1†) obtained by using six N719 standards from 0 to 1.0 mM (11.82 mM^{-1} cm^{-1}).[29]

The equilibrium N719 adsorption capacity of N719 was measured for freely dispersed P25, P25/ZnO_2 powder at seven N719 concentrations (25–500 mg L^{-1}) at 22, 40 and 50 °C. The

adsorbed dye (q) (mg g^{-1}) was calculated according to eqn (1) (ref. 30)

$$q = (C_0 - C_e)V/m \quad (1)$$

where C_0 (mg L^{-1}) and C_e (mg L^{-1}) are the initial and equilibrium N719 concentrations (mol L^{-1}), respectively, V is the volume of dye solution (L), and m is the TiO_2 mass (mg). Fits to the Langmuir (eqn (2))[31] or Freundlich isotherms (eqn (3) and (4))[31,32] were then calculated by plotting the data according to the relevant equations. For Langmuir,

$$C_e/q = 1/K_L q_m + C_e/q_m \quad (2)$$

where C_e is the equilibrium N719 concentration (mg L^{-1}), q is the equilibrium adsorption capacity (mg g^{-1}), q_m is the maximum adsorption capacity (mg g^{-1}) and K_L (L mg^{-1}) is the Langmuir constant. For Freundlich, eqn (3) was converted to the linear form (eqn (4)).

$$q_e = K_f C_e^{1/n} \quad (3)$$

$$\ln q_e = \ln K_f + 1/n \ln C_e^{1/n} \quad (4)$$

where q_e is the equilibrium adsorbate concentration (mg g^{-1}), K_f is the Freundlich constant (mg g^{-1}), C_e is the equilibrium solution concentration (mg l^{-1}), and $1/n$ represents the dimensionless heterogeneity factor.

Results and discussion

To emphasise the importance of the binder within the pastes, two P25/terpineol pastes were prepared; one with ethyl cellulose binder and one without binder. These were doctor bladed onto glass microscope slides and oven sintered at 450 °C for 30 min. Fig. 1 initially suggests that the resultant films appear similar. However, a closer inspection of the binder-free film reveals fine cracks and a simple adhesion test of applying Scotch tape to the film and removing it shows that the TiO_2 film arising from the binder-free paste delaminates easily (as denoted by the dashed red box in Fig. 1) whilst the film from the binder-containing paste remains strongly adhered to the glass substrate.

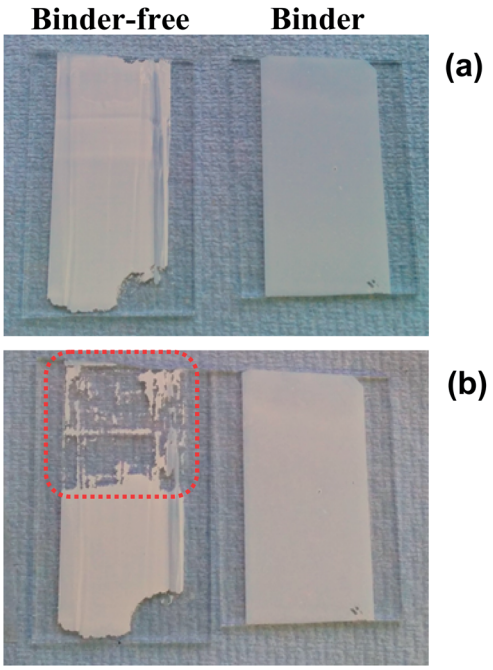

Fig. 1 Photographs of films produced by sintering either binder-free or binder-containing P25 pastes at 450 °C for 30 min; (a) as produced films and (b) after the adhesion test using Scotch tape. Binder = ethyl cellulose.

Thermal chemistry

The approach taken in this paper is to lower the sintering temperature of binder-containing pastes by including metal peroxide powders which decompose to produce metal oxide particles and release oxygen and heat within the photo-electrode film during the sintering process.

Detailed thermal analyses of selected pastes used in this study are shown in Fig. 2 (all the data are shown in ESI Fig. 2†). These TGA/DSC data can be used to explain the principle of the metal peroxide combustion effect. In addition, the challenge of lowering the sintering temperature of metal oxide pastes can be understood by looking at the detailed thermal analysis of a P25 paste (Fig. 2a). The data show a three-stage weight loss for P25-only pastes with an initial loss of terpineol solvent (*ca.* 70%) between 60 °C and 214 °C which is associated with an endothermic peak which reaches its minimum at *ca.* 190 °C in line with that this is an evaporative rather than a combustion process. The second weight loss (*ca.* 10%, 210–320 °C) is associated with a broad, multi-feature exotherm with a shoulder at *ca.* 240 °C (labelled Ia in Fig. 2a) and two maxima at *ca.* 290 and 320 °C. These features are associated with the combustion of ethyl cellulose to $CO_{2(g)}$ and $H_2O_{(g)}$. Although the final weight loss is small (3%, 320–450 °C), it is associated with a strong exothermic peak (maximum at *ca.* 410 °C) which continues up to 450 °C (labelled IIIa in Fig. 2a). This is ascribed to the combustion of the residual carbonaceous material from the ethyl cellulose binder which, if not combusted, is believed to reduce dye uptake by blocking surface sorption sites. This residual organic matter gives rise to the brown colouration in under-sintered films (see Fig. 3). It is key to remove this material to prepare suitable metal oxide surfaces for dyeing. The reason for adding the metal peroxides to the paste is to introduce an oxygen source and heat during binder combustion to accelerate the removal of this residual organic matter.

As such, an initial screening of P25 pastes containing metal peroxides involved mixing either calcium, magnesium or zinc peroxide into a P25/terpineol paste containing ethyl cellulose binder at a loading of 5, 10 or 15% by wt *versus* P25. After casting onto glass slides, the films were sintered up to 250–300 °C for 30–120 min. Fig. 3 shows that, after 30 min at 300 °C, the P25 control film changes from yellow to brown. Further tests show that the P25-only film becomes white only after heating to 450 °C; this colour change was deemed to be a suitable visual indicator of complete binder combustion which would prepare

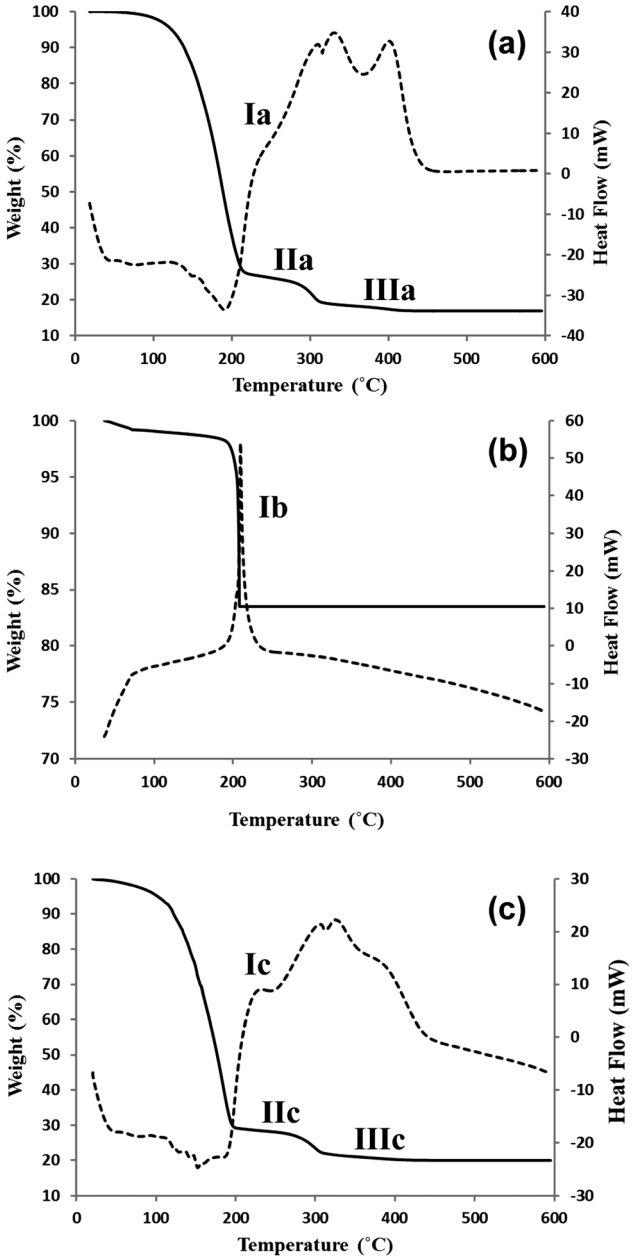

Fig. 2 TGA/DSC data for (a) P25 paste, (b) ZnO_2 powder and (c) P25/ZnO_2 paste heated from RT to 600 °C at 10 °C min^{-1}. TGA = solid lines and DSC = dashed lines. Exotherm = up.

the metal oxide surface area for dyeing. The films from the metal peroxide pastes all show some residual pale brown colour at combustion temperatures up to 250 °C regardless of the metal peroxide loading (see ESI Fig. 3†). At 250 °C, the P25/CaO_2 film appeared paler than the other films after 30 min but increasing the sintering time up to 120 min did not change this. However, sintering these films at 300 °C for 30 min produces white films for all the P25/peroxide films whilst the P25-only control film remains brown (Fig. 3). Hence, 300 °C was considered to be the threshold temperature to initiate both metal peroxide decomposition (MO_2 becoming MO and $1/2O_2$) and binder combustion.

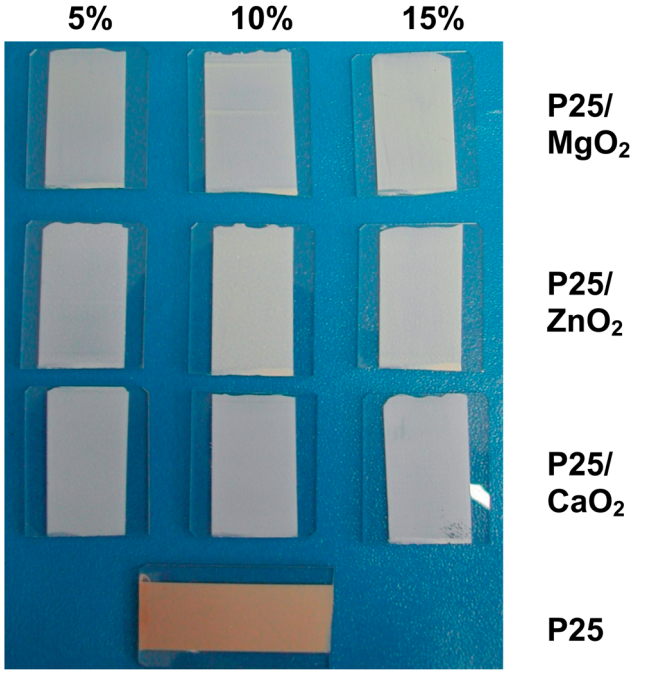

Fig. 3 Photograph of films (*ca.* 3 × 2 cm) prepared from P25 and P25/peroxides (5–15% w/w) binder-containing pastes after sintering for 30 min at 300 °C.

To explore the reasons for the beneficial effects of metal peroxides in detail, further TGA/DSC data have been recorded. All the data are presented in ESI Fig. 2† whilst only the selected data for ZnO_2 are presented here as these data are representative of all the different metal peroxides tested. Thus, TGA/DSC data for powdered ZnO_2 (Fig. 2b) show a small weight loss (*ca.* 2%) for up to 190 °C and then a very rapid weight loss of *ca.* 16% centred around 200 °C which corresponds to the decomposition of ZnO_2 into ZnO (eqn (5)). This is accompanied by a sharp exothermic peak which is labelled Ib in Fig. 2b. This is important because the ZnO_2 decomposition occurs at a slightly lower temperature than the temperature at which binder combustion commences (see IIa in Fig. 2a). This means that the heat or oxygen released from ZnO_2 decomposition will be available to enhance binder combustion at lower temperatures. In addition, because the metal peroxide particles are mixed into pastes, they are subsequently distributed through the printed and sintered films. Hence, as the metal peroxides decompose, they release oxygen and heat to their local environment where the binder residues exist. This reduces any mass transfer issues which further helps to explain the enhanced binder combustion at lower temperatures.

$$ZnO_{2(s)} \rightarrow ZnO_{(s)} + 1/2O_{2(g)} \quad (5)$$

These effects are illustrated by the data for a P25/ZnO_2 paste (Fig. 2c). As expected, the data show a very similar pattern to the P25 paste because the paste only contains 10% ZnO_2. However, there is a much more clearly defined and more intense exothermic peak in the DSC signal (labelled Ic in Fig. 2c). This reflects the exothermic process associated with ZnO_2

decomposition. As predicted, this is believed to have two main effects; firstly additional and localized heat is released within the film and secondly the peroxide decomposing releases oxygen into the film which can help to oxidize the organic binder. This results in a greater loss of residual organic matter from the film at temperatures lower than 450 °C (labelled IIIc in Fig. 2c). By comparison, the TGA/DSC data for CaO_2 and MgO_2 (see ESI Fig. 2†) show that, while they decompose to produce CaO and MgO, respectively and to release oxygen, the main weight loss takes place at a higher temperature (*ca.* 400 °C). Also, for both CaO_2 and MgO_2, their decomposition is an endothermic process which will remove energy from the surrounding paste during sintering. Thus, for these peroxides, the localized addition of oxygen should still occur at similar temperatures for binder combustion and therefore should still help this process. However, during any sintering process, the paste must be heated from room temperature to the sintering dwell temperature. Hence, the higher decomposition temperatures for CaO_2 and MgO_2 mean that oxygen will be released slightly later in the process. Overall, both the higher temperature and endothermic nature of the decomposition mean that CaO_2 and MgO_2 should be less effective combustion additives compared to ZnO_2.

Having established that the addition of metal peroxides can reduce the sintering temperature of TiO_2–ethyl cellulose pastes, selected films were sintered at different temperatures and sensitized with N719 before being manufactured into dye-sensitized solar cell devices as described in the next section.

DSC device data

In this paper, we study sintering and so we have made larger photo-electrodes (1 cm^2) than are typically reported for DSC devices to test film cohesion in devices.[33] To study the reproducibility, we have also made replicate devices and reported the average $\eta \pm$ the error. Whilst this suppresses device efficiencies relative to the highest efficiencies reported in the literature (*e.g.* for ball-milled P25 pastes[34,35]), this approach is necessary to accurately test the effectiveness of the different sintering treatments.

Table 1 shows *IV* data for replicate devices made using one layer of metal oxide paste (*ca.* 7 μm thickness) after sintering at 300 or 450 °C. The approach taken was to keep the photo-electrode thickness constant and vary the type of TiO_2 particles used in the paste. This was because DSC devices tend towards thinner electrodes as the molar extinction coefficient (ε) of dyes increases and because solid state devices require thinner electrodes. Thus, two different pastes have been studied in these devices; an in house prepared P25-ethyl cellulose-terpineol paste which is denoted as P25 in Table 1 and a commercial TiO_2 paste (DSL18NR-T from Dyesol Ltd) which is denoted as NRT in Table 1. The data for the TiO_2-only films P25 sintered at 450 °C can be used as a baseline for the other devices. Thus, Device A for P25-only shows a η of 4.4% with a J_{sc} of 9.01 mA cm^{-2} and a V_{oc} of 0.71 V. By comparison, Device B gives a better performance ($\eta = 5.0\%$) mainly due to an improvement in J_{sc} up to 9.80 mA cm^{-2}. This is ascribed to the DSL18NR-T paste containing smaller, nanoparticulate anatase TiO_2 particles leading to higher dye loading (see ESI Fig. 4†). In addition the DSL18NR-T paste contains no rutile phase whilst P25 does which is known to produce less efficient DSC devices.[36] The DSL18NR-T paste has also been optimized for DSC devices.

Table 1 *IV* data for (1 cm^2) N719-dyed DSC devices prepared using P25 or P25/peroxide pastes (10% wt/wt). Efficiencies are reported as the mean of 3 devices for each condition ± error

	Paste	$TiCl_4$	η (%)	FF	V_{oc}/V	J_{sc}/mA cm^{-2}
450 °C						
A	P25	Yes	4.4 ± 0.2	0.69	0.71	9.01
B	NRT	Yes	5.0 ± 0.2	0.65	0.79	9.80
C	P25/CaO_2	Yes	3.4 ± 0.1	0.61	0.78	6.85
D	P25/MgO_2	Yes	3.5 ± 0.1	0.57	0.78	7.99
E	P25/ZnO_2	Yes	4.4 ±0.1	0.73	0.78	7.73
F	NRT/ZnO_2	Yes	5.7 ± 0.2	0.72	0.77	10.43
300 °C						
G	P25	Yes	0.3	0.61	0.58	0.82
H	P25	No	0.0	0.34	0.02	0.20
I	P25/CaO_2	Yes	3.2 ± 0.2	0.55	0.79	7.32
J	P25/MgO_2	Yes	3.5 ± 0.1	0.53	0.78	8.32
K	P25/ZnO_2	Yes	4.1 ± 0.2	0.72	0.77	7.51
L	P25/ZnO_2	No	1.1 ± 0.0	0.60	0.74	2.53
M	NRT/ZnO_2	Yes	5.7 ± 0.1	0.71	0.76	10.62
N	NRT/ZnO_2	No	0.0 ± 0.0	0.00	0.01	0.02
O[a]	NRT/ZnO_2	Yes	7.5 ± 0.3	0.67	0.84	13.40

[a] Cocktail dyed (N719/SQ1) 0.26 cm^2 device.

For the P25/peroxide films sintered at 450 °C, the highest efficiencies are observed for the ZnO_2 treated pastes. Thus, for P25/ZnO_2 (Device E) $\eta = 4.4\%$ which is comparable to the P25-only device (Device A). By comparison, the NRT/ZnO_2 data (Device F) again show a significant improvement over the P25 and P25/ZnO_2 data with $\eta = 5.7\%$ which is again mainly due to the improved J_{sc}. However, the NRT/ZnO_2 device also shows a significant improvement compared to Device B which contains only DSL18NR-T with improved efficiency again related to the improved J_{sc}. This is in line with the P25 data which suggest that ZnO_2 provides an additional benefit to the device performance. This may be because the larger ZnO_2 particles may increase light scattering during device operation and/or that the ZnO_2 particles provide an additional benefit during sintering leading to an improved surface area and dye loading. Having established the influence of peroxides on larger devices, some smaller (0.26 cm^2) devices were prepared and ultra-fast dyed with N719/SQ1 cocktail solution[27] to study the effect of increased J_{sc} on the peroxide photo-electrodes. This showed that device efficiencies of up to $\eta = 7.5\%$ can be achieved from a binder-containing paste sintered at 300 °C (Table 1) which is comparable with previous reports for this dye system.[27] To the best of our knowledge, the performance of these devices is comparable to the highest efficiency devices reported for DSCs fabricated using low temperature methods except that the previous reports used binder-free TiO_2 pastes and pressure rather than thermal sintering.[18,19]

Sintering the photo-electrodes at 300 °C shows the importance of the metal peroxide additions. For example, sintering P25-only devices at 300 °C gives very low η regardless of whether $TiCl_4$ treatment is used ($\eta < 0.3\%$, Devices F and G); essentially resulting in non-functional devices. Sintering DSL18NR-T pastes which do not contain ZnO_2 at 300 °C produces similar device performances; *i.e.* no efficiency (data not shown). By comparison, sintering P25/metal peroxide films at 300 °C shows similar device performance data to the respective 450 °C sintered films. The highest efficiency for these devices is again observed for $P25/ZnO_2$ compared to $P25/CaO_2$ or $P25/MgO_2$ (Device J *versus* Devices H and I).

The data also show the importance of $TiCl_4$ treatment for the metal peroxide-containing films. For $P25/ZnO_2$ pastes, the $TiCl_4$ treatment increases η from 1.1% (Device L, no $TiCl_4$) to 4.1% (Device K, with $TiCl_4$). For the DSL18NR-T/ZnO_2 paste, the effect is even more pronounced with zero η without $TiCl_4$ treatment (Device N) and $\eta = 5.7\%$ with $TiCl_4$ (Device M). For DSL18NR-T, it is hard to compare the data as the absence of $TiCl_4$ produces a non-functional device. However, for the $P25/ZnO_2$ devices, the main reason is $J_{sc.}$ This effect is ascribed to the $TiCl_4$ treatment hydrolyzing onto the photo-electrode surface producing a more coherent TiO_2 surface for dyeing. Indeed, it is known that $TiCl_4$ treatment has little influence on high temperature sintered devices where all organic matter has been removed and the particles are thermally well sintered together. However, it is noteworthy that the $TiCl_4$ treatment effectively repairs photo-electrode defects. The differences in performance between the P25 and DSL18NR-T pastes may reflect different paste additives which make it more difficult to remove all organic matter from the commercial paste at 300 °C. To illustrate the importance of J_{sc}, EQE_{max} for N719 at 530 nm for a P25 device sintered at 450 °C is shown in Fig. 4. By comparison of films sintered at 300 °C, the $P25/ZnO_2$ device shows an EQE of 45% at 530 nm whilst the equivalent P25-only device shows an EQE of <5%. Finally, the data for NRT/ZnO_2 sintered at 300 °C (Device M) shows very similar data to the equivalent device sintered at 450 °C with $\eta = 5.7\%$; again an improvement over the NRT-only device sintered at 450 °C (Device B).

Transient photovoltage and photocurrent decay measurements have been used to further study the influence of sintering temperature, $TiCl_4$ treatment and ZnO_2 addition to devices (Fig. 5 and ESI Fig. 5†). The data show significantly longer recombination lifetimes for all $TiCl_4$ treated photo-electrodes compared to their non-$TiCl_4$ treated analogues. For P25 devices, there is no difference in the transport kinetics which suggests that any increase in J_{sc} observed as a result of $TiCl_4$ treatment can be attributed to a downward shift in the conduction band as observed in ref. 37. For the 300 °C sintered devices however, an apparent decrease in transport kinetics, due to $TiCl_4$ treatment, may indicate a change in trap density additional to the negative CB shift that is commonly observed as a result of $TiCl_4$ treatment. The large decrease in the recombination rate observed in devices made with ZnO_2 paste suggests that the ZnO_2 performs a different role from $TiCl_4$ in the devices and supports our assertion that the peroxide assists in binder combustion and the removal of the residual organic material which otherwise acts as recombination sites. The data also show that the 450 °C sintered P25 device without ZnO_2 or $TiCl_4$ treatment shows comparable recombination lifetimes to $TiCl_4$-treated devices suggesting that $TiCl_4$ treatment does not significantly affect recombination processes for well-sintered TiO_2-only photo-electrodes which is in line with many literature reports. However, recombination lifetimes shorten for the 450 °C sintered ZnO_2/P25 device without $TiCl_4$ treatment but are the shortest for all the 300 °C sintered devices which have not been

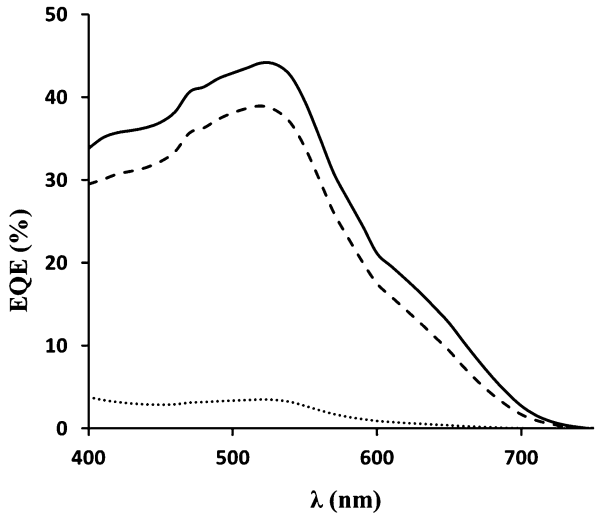

Fig. 4 EQE of P25 films sintered at 300 °C (dotted line), 450 °C (dashed line), and $P25/ZnO_2$ (solid line) sintered at 300 °C for 30 min. All films were $TiCl_4$ treated and dyed with N719.

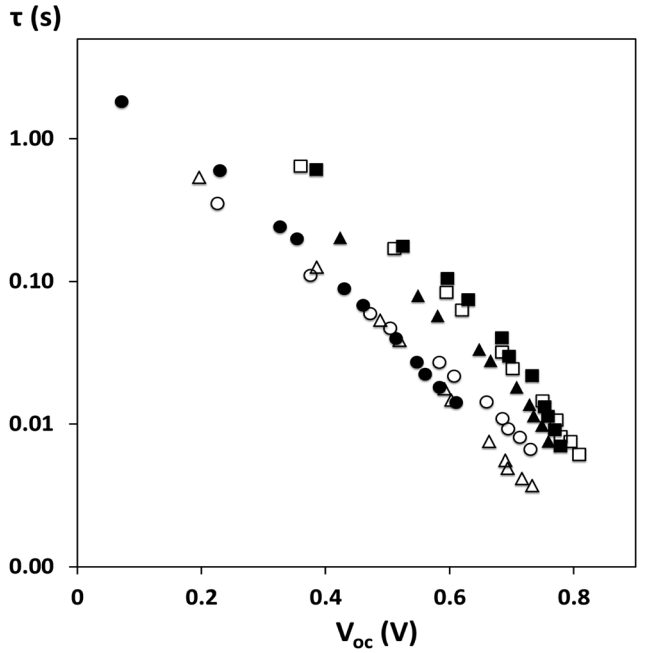

Fig. 5 Recombination lifetime τ *versus* V_{oc} for devices sintered at 450 °C – ■ P25 with $TiCl_4$; ▲P25 no $TiCl_4$ or at 300 °C – ○ P25 with $TiCl_4$; Δ P25 no $TiCl_4$; □ ZnO_2/P25 with $TiCl_4$; ● ZnO_2/P25 no $TiCl_4$.

$TiCl_4$ treated. These data confirm that both ZnO_2 and $TiCl_4$ treatment are required for low temperature sintering to achieve adequate recombination lifetimes for effective charge extraction. Overall, these data show that low temperature sintering of binder-containing TiO_2 pastes is possible and with careful control to minimize any over-sintering of the TiO_2 surface can lead to enhanced short-circuit currents. The later materials characterisation work reported in this paper has sought to understand the reasons for these observations.

Studies of varying the ZnO_2 paste loading from 5 to 25% show that a lower ZnO_2 loading (5–10%) gives the best device performance (see ESI Table 1†). This is mainly due to reduced J_{sc} as the metal peroxide loading increases which is ascribed to lower dye loadings arising from an increased proportion of lower surface area ZnO_2 particles. Studies of extending the sintering time at 300 °C from 30 min to 120 min (see ESI Table 2) also show a slight negative impact on the device efficiency due to slight reduction in J_{sc} and V_{oc}. These changes probably reflect the increased interactions between the zinc oxide and TiO_2 phases with time which may lead to a loss of surface area and potentially the surface doping of each phase into the other.

Materials characterisation

The aim of this part of the work is to try to understand how the addition of metal peroxides to TiO_2-ethyl cellulose pastes affects the phases and morphology of the resulting metal oxides. Their surface chemistry has also been studied using BET and dye loading isotherms because of the strong correlation between device performance and J_{sc}. Thus, a key aim of this work is to understand if the completion of sintering and any presence of residual organic matter is linked to the surface area and dye loading. Unless otherwise stated, the data for P25-ethyl cellulose pastes containing 10% ZnO_2 (by wt) are presented as these pastes gave rise to the most efficient DSC devices.

First, looking at the structural phases present, XRD data show that all the films contain anatase[38] and rutile[39] TiO_2 phases in an approximately 4 : 1 ratio as expected for the P25 film. The data for a sintered P25/ZnO_2 film (Fig. 6) show additional peaks at 31.7° and 34.4° 2θ, which can be attributed to ZnO[40] resulting from the decomposition of ZnO_2. The data for P25/CaO_2 or P25/MgO_2 films were essentially identical to the P25-only film with no evidence for the formation of a second metal oxide phase which suggests that the CaO_2 or MgO_2 forms amorphous products on decomposition (see ESI Fig. 6†). The P25-only XRD data also show a slight narrowing of the diffraction lines (see ESI Fig. 6 and 7†) for films sintered at 450 °C compared to the films sintered at 300 °C which is in line with the increased crystallinity and inter-particle necking. Interestingly, a similar but subtle effect is observed for the P25/peroxide films sintered at 300 °C. It is difficult to identify the reasons for this with absolute confidence because XRD measures an "average" across the whole sample. However, this might reflect the generation of localized heat during peroxide decomposition as the TGA shows that this is an exothermic process. In turn, this might increase the TiO_2 crystallinity and/or might reflect increased inter-particle interactions leading to an increased crystallite size.

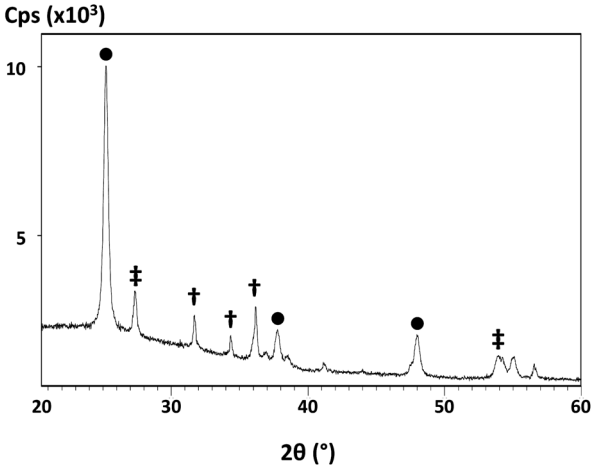

Fig. 6 X-ray diffraction pattern of a P25/ZnO_2 film sintered at 300 °C showing ● anatase TiO_2, ‡ rutile TiO_2 and † ZnO.

SEM data (Fig. 7) clearly show two different types of particles interspersed within the film. The majority of particles are *ca.* 25 nm in size and the EDX analysis (see ESI Fig. 8†) shows the presence of Ti and O confirming these as P25 TiO_2 nanoparticles (Fig. 7 – top). The data also show larger irregularly shaped agglomerations of particles which are 100–300 nm in size and the EDX data of these particles show the presence of Zn and O, confirming these to be the ZnO particles arising from the thermal decomposition of ZnO_2. Interestingly, the surface morphology of particles appears different depending on the sintering temperature. Thus, after sintering at 450 °C, the surface appears smooth and the particles appear to be singular whilst the 300 °C sintered particles are larger (120–600 nm), have a much more irregular surface and appear to be made up of many smaller particles. This suggests that, whilst the TGA data show that the loss of O_2 from the ZnO_2 occurs rapidly at *ca.* 200 °C, the atomic rearrangement into a more ordered ZnO structure is not complete after 30 min at 300 °C.

Sorption data have been measured either using $N_{2(g)}$ sorption data at −196 °C fitted to the BET model isotherm or using N719 dye solutions sorbed at 22, 40 or 50 °C which have been fitted to the model Langmuir or Freundlich isotherm. The dye

Table 2 Parameters derived from Langmuir isotherms of N719 dye at 22, 40 or 50 °C on the P25 film sintered at 450 °C or on P25/ZnO_2 films sintered at 300 or 450 °C

Paste	Dyeing temp. (°C)	q_m (mg g^{-1})	K_L (l mg^{-1})	R_L	R^2
P25 (450 °C)	22	47.5	0.021	0.088	0.999
	40	76.6	0.022	0.082	0.998
	50	85.9	0.030	0.050	0.998
P25/ZnO_2 (450 °C)	22	62.1	0.023	0.081	0.999
	40	88.4	0.029	0.064	0.998
	50	106.3	0.038	0.050	0.997
P25/ZnO_2 (300 °C)	22	70.9	0.029	0.064	0.997
	40	94.8	0.040	0.048	0.997
	50	116.2	0.044	0.043	0.997

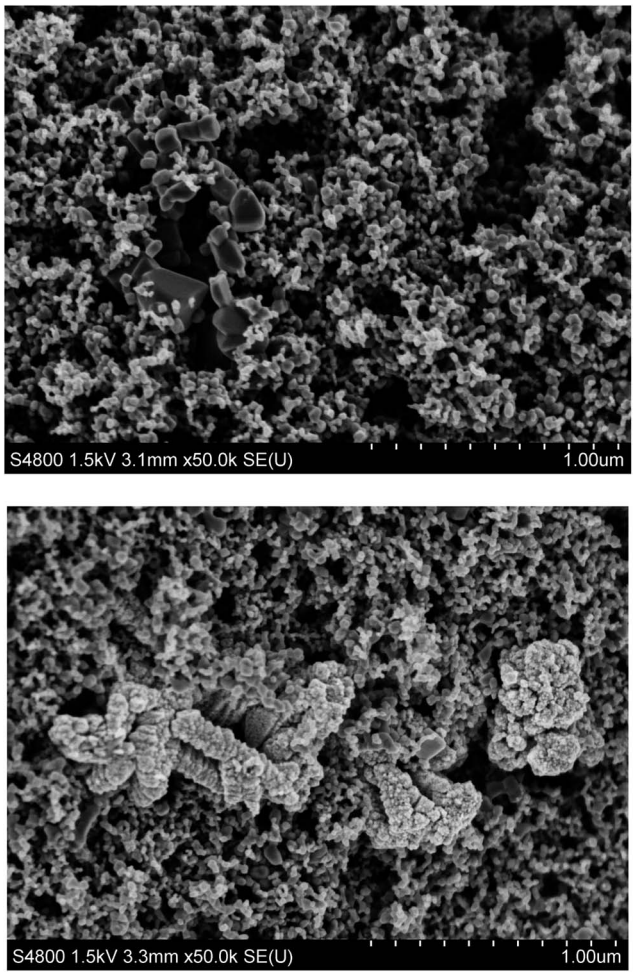

Fig. 7 Scanning electron micrographs of ZnO_2-containing P25 films sintered at (top) 450 °C and (bottom) 300 °C.

uptake data have been measured using relatively low initial dye concentrations passively dyed and at equilibrium to study the effects of photo-electrode composition ($\pm ZnO_2$) and sintering conditions (300 *vs.* 450 °C) rather than to optimise sensitization. Thus, fast dyeing[27] higher initial dye concentrations would be expected to show different responses but that is beyond the scope of this paper. P25/ZnO_2 films were chosen as these devices show the best device responses compared to the P25 or other P25/peroxide films (Table 1).

The N_2 sorption BET data show a surface area of 54 m^2 g^{-1} for P25 sintered a 300 °C which drops to 45 m^2 g^{-1} after sintering at 450 °C. This is expected because one aim of raising the temperature to 450 °C is to sinter particles together and create inter-particle necking. This can only be achieved if the TiO_2 surface atoms become mobile. If this occurs, then the surface tension will provide a driving force towards smoothing the surface to the lowest surface area. In this case, 450 °C is not sufficient to complete this process but is sufficient to sinter the particles together. For the P25/ZnO_2 data, a similar trend is observed but with a surface area of 51 m^2 g^{-1} at 300 °C and 42 m^2 g^{-1} at 450 °C. The situation is complicated for these samples partly because they contain a mixture of TiO_2 particles along with a smaller number of ZnO particles which have resulted from the decomposition of ZnO_2 but also because the surface area measurement is an average across the whole. Looking at neat ZnO_2 powder first, this has a surface area of 14 m^2 g^{-1} at RT which increases slightly to 18 m^2 g^{-1} after sintering at 300 °C but drops to 7.8 m^2 g^{-1} at 450 °C. These trends are typical for a material such as ZnO_2 which releases gas during decomposition as this effectively bursts out of the material creating an increased surface area during the process.[41] However, the resultant ZnO particles sinter rapidly as the temperature is increased further to 450 °C resulting in a subsequent loss of surface area. Thus, whilst the "average" surface area of P25/ZnO_2 might be expected to be slightly lower to reflect the addition of lower surface area ZnO_2 particles, it is not possible to separate out what is happening to the surface of the TiO_2 particles alone. In addition, N_2 will physisorb to residual organic matter and also include this surface area in the data whilst N719 dye will only chemisorb to "free" metal oxide surfaces. Finally, N_2 is much smaller than N719 and so their sorption characteristics will be different. Hence, although the BET data are useful in highlighting trends between organic matter containing under-sintered samples and over-sintered samples (where the surface area begins to be lost), dye loading data have been measured and analysed in some detail to provide the most accurate picture of the metal oxide surface for dye binding.

The dye sorption data show relatively higher dye sorption at a low initial dye concentration. However, as the initial dye concentration increases, dye sorption increases but to a relatively lesser extent until the data reach a plateau (Fig. 8 – top). This is expected as there are a fixed number of sorption sites in the metal oxide films and, as these become increasingly filled fewer free sites remain, and greater dye concentrations are required to partition more dye on the surface. However, in these measurements, the dye concentration decreases throughout the experiment as the dye adsorbs until equilibrium is reached between the remaining free sites and the remaining dye concentration. Thus, if the dye concentration is proportional to the driving force for dye sorption and this drops throughout the sorption process, the initial dye concentration should be predictive of the final dye loading.

Comparing the two isotherm models, the R^2 values are consistently higher when the data are fitted to the Langmuir isotherm ($R^2 > 0.997$) compared to the Freundlich isotherm (R^2 0.962–0.983); see ESI Fig. 9–11 and ESI Tables 3–6.† The Langmuir model assumes monolayer sorption of adsorbates onto identical sites in separate sorption events whilst the Freundlich model assumes that adsorption takes place on heterogeneous surfaces and is not restricted to monolayer sorption.[33] On the basis of the higher correlations, the Langmuir data have been used to analyse dye uptake using P25 films sintered at 450 °C as a control to compare to P25/ZnO_2 films sintered at either 450 or 300 °C.

First comparing the data for P25 and P25/ZnO_2 films sintered at 450 °C, the values for adsorption capacity (q_m) are consistently higher for the P25/ZnO_2 films which is in line with the higher J_{sc} of these devices (Table 2). This is despite the

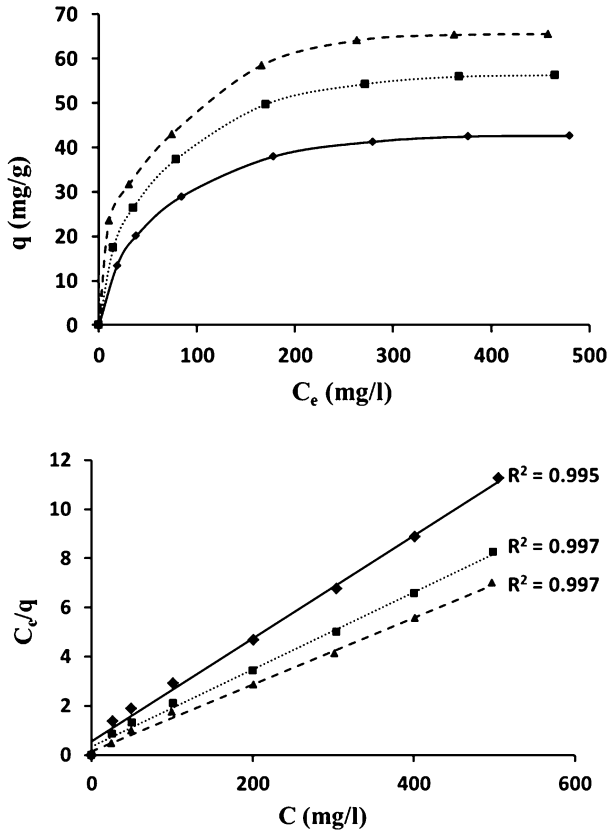

Fig. 8 (Top) Adsorption isotherms of N719 dye at 22 °C on (solid line, diamonds) P25 sintered at 450 °C; (dotted line, squares) P25/ZnO_2 sintered at either 450 °C or (dashed line, triangles) at 300 °C and (bottom) the same data fitted to Langmuir isotherms.

slightly lower surface area of the P25/ZnO_2 films measured by N_2 sorption. As discussed previously, the N_2 BET data measure an "average" surface area of the entire sample surface (TiO_2, ZnO and any residual organic matter). However, we expect the dye sorption data to only measure a monolayer of N719 dye chemisorbed to any available metal oxide surfaces. Thus, we believe the increased dye loading in P25/ZnO_2 samples reflects the improved removal of residual organic matter from the metal oxide surfaces that improves the metal oxide surfaces for dye uptake. However, the device efficiency data (ESI Table 1†) show that increasing the ZnO_2 loading in the films from 5 to 15 to 25% reduces the device performance. This suggests that the increases in dye uptake are associated with improvements in the surface of TiO_2 particles. This is in line with earlier assertions that the main role of ZnO_2 is to release oxygen and heat to aid binder combustion which removes organic matter and increases the TiO_2 surface area for dye binding.

The data in Table 2 also show that adsorption capacity is higher for P25/ZnO_2 films sintered at 300 °C than P25 or P25/ZnO_2 films sintered at 450 °C. This is to be expected based on the higher BET surface area of P25/ZnO_2 films sintered at 300 °C. However, as discussed previously, the situation is complicated because the BET data are an average of all the material data in the sample. The increased dye uptake for P25/ZnO_2 at 300 °C suggests that the presence of ZnO_2 results in greater removal of residual organic matter from metal oxide surfaces (which in this sample must be dominated by the much more abundant TiO_2 particles). In addition, the higher BET surface area and increased dye loading after 300 °C sintering suggest that, as long as the residual binder can be removed at lower temperature, the metal oxide particles lose less surface area than if sintered at 450 °C. However, this benefit can only be realised with increased dye loading if a combustion agent such as ZnO_2 is added to help combust the residual binder. This beneficial influence on dye loading has not been realised before because it has not been previously been possible to sinter binder-containing pastes at low temperature.

Table 2 also shows that the N719 adsorption capacity increases on all films with dyeing temperature which suggests an endothermic adsorption process. In practice, solvent volatility limits the dyeing temperature and so these data have only been measured up to 50 °C. Low R_L values indicate favourable dye uptake.[30] The data show that R_L values decrease with increasing dyeing temperature and also across the series P25 450 °C > P25/ZnO_2 (450 °C) > P25/ZnO_2 (300 °C). Thus, P25/ZnO_2 films sintered at 300 °C and dyed at 50 °C show the most favourable N719 uptake in line with the highest N719 adsorption capacity. This is in line with the J_{sc} and η data which suggests that, as expected, J_{sc} is linked to dye loading (Table 1).

Conclusions

The data show that, for the first time, binder-containing pastes can be sintered at low temperature by using metal peroxide combustion promoters. This has the advantage that metal peroxides are low cost powders which are safe and easy to use with commonly used paste formulations. The most effective metal peroxide when using ethyl cellulose binder-containing pastes is ZnO_2 which is believed to be because ZnO_2 decomposes at similar temperatures to ethyl cellulose combustion so that the oxygen released during this process enhances binder combustion and removal as $CO_{2(g)}$ at lower temperature. In addition, the by-products of ZnO_2 decomposition are relatively large particles of ZnO which may enhance light scattering within the device whilst not limiting the device performance because ZnO is used as a photo-anode material in DSC devices in its own right.

The sorption data show the importance of considering BET surface area data arising from multi-layer N_2 physi-sorption as the average of the whole sample surface area whilst dye loading data relate to chemisorbed dye monolayers. Furthermore, dye loading data after sintering at lower temperatures show, for the first time, that this can actually give rise to higher dye loadings which is linked to the removal of the residual binder at lower temperatures along with a reduction in the loss of metal oxide surface area associated with 450 °C sintering. This suggests that sintering at 450 °C actually slightly over-sinters TiO_2 resulting in a loss of surface area and lowered dye loading. However, it remains important to remove the vast majority (and ideally all) of the organic binder in order to maximize the number of dye binding sites and resulting J_{sc}. Thus, a general model of sintering would be to sinter at the lowest possible temperature to

remove the organic material, optimize dye loading and enable the formation of inter-particle connections to ensure the films are mechanically robust.

Acknowledgements

We gratefully acknowledge the Iraqi Govt. support for DKM, ERDF-WG LCRI funding for SPARC (AC, EWJ, CC), EPSRC SPECIFIC funding (MLD) and Sêr Cymru funding (PJH), Drs Graham Ormondroyd and Simon Curling in the Biocomposites Centre for BET measurements and NSG for the supply of TEC™ glass to the SPARC consortium.

Notes and references

1 B. O'Regan and M. Grätzel, *Nature*, 1991, **353**, 24.
2 C. J. Barbé, F. Árendse, P. Comte, M. Jirousek, F. Lenzmann, V. Schlover and M. Grätzel, *J. Am. Ceram. Soc.*, 1997, **80**, 3157–3171.
3 N. Park, J. van de Lagemaat and A. Frank, *J. Phys. Chem. B*, 2000, **104**, 8989–8994.
4 M. Grätzel, *J. Sol-gel Sci. Technol.*, 2001, **22**, 7–13.
5 L. M. Gonçalves, V. de Zea Bermudez, H. A. Ribeiro and A. M. Mendes, *Energy Environ. Sci.*, 2008, **1**, 655–667.
6 P. J. Holliman, M. L. Davies, A. Connell, M. J. Carnie and T. M. Watson, in *Functional Materials for Energy Applications*, ed. J. A. Kilner, S. J. Skinner, S. J. C. Irvine and P. P. Edwards, Woodhead Publ., Cambridge, 2012, ISBN-13: 978 0 87509 059 1.
7 J. Nelson, *Phys. Rev. B: Condens. Matter Mater. Phys.*, 1999, **59**, 15374–15380.
8 S. Ito, N.-L. Cevey Ha, G. Rothenberger, P. Liska, P. Comte, S. M. Zakeeruddin, P. Péchy, M. K. Nazeeruddin and M. Grätzel, *Chem. Commun.*, 2006, 4004–4006.
9 K. Miettunen, J. Halme and P. Lund, *WIREs Energy Environ.*, 2013, **2**, 104–120.
10 Y. Kijitori, M. Ikegami and T. Miyasaka, *Chem. Lett.*, 2007, **36**(1), 190–191.
11 F. Pichot, J. R. Pitts and B. A. Gregg, *Langmuir*, 2000, **16**, 5626–5630.
12 T. M. Paronyan, A. Kechiantz and M. Lin, *Nanotechnology*, 2008, **19**, 115201.
13 D. Zhang, T. Yoshida, K. Furuta and H. Minoura, *J. Photochem. Photobiol., A*, 2004, **164**, 159–166.
14 C. Li, Y. Lin, X. Li, Z. Wang, Y. Ma, X. Zhou, S. Feng and X. Xiao, *Chin. Sci. Bull.*, 2005, **50**, 1449–1452.
15 Y. Xiao, J. Wu, Q. Li, G. Xie, G. Yue, H. Ye, Z. Lan, M. Huang and J. Lin, *Chin. Sci. Bull.*, 2010, **55**, 980–985.
16 D. Gutiérrez-Tauste, I. Zumeta, E. Vigil, M. A. Hernández-Fenollosa, X. Domènech and J. A. Ayllón, *J. Photochem. Photobiol., A*, 2005, **175**, 165–171.
17 D. Zhang, T. Yoshida, T. Oekermann, K. Furuta and H. Minoura, *Adv. Funct. Mater.*, 2006, **16**, 1228–1234.
18 T. Yamaguchi, N. Tobe, D. Matsumoto, T. Nagai and H. Arakawa, *Sol. Energy Mater. Sol. Cells*, 2010, **4**, 812–816.
19 T. Yamaguchi, N. Tobe, D. Matsumoto and H. Arakawa, *Chem. Commun.*, 2007, 4767–4769.
20 S. Senthilarasu, T. A. Nirmal Peiris, J. Garcia-Canadas and K. G. Upul Wijayantha, *J. Phys. Chem. C*, 2012, **116**, 19053–19061.
21 A. G. Agrios and A. Hagfeldt, *J. Phys. Chem. C*, 2008, **112**, 10021–10026.
22 Li, J. Li, N. Wang, C. Lin and L. Zhang, *J. Photochem. Photobiol., A*, 2008, **195**, 247–253.
23 T. Kado, M. Yamaguchi, Y. Yamada and S. Hayase, *Chem. Lett.*, 2003, 1056–1057.
24 H. Kim, R. Auyeung, M. Ollinger, G. Kushto, Z. Kafafi and A. Piqué, *Appl. Phys. A: Mater. Sci. Process.*, 2006, **83**, 73–76.
25 S. Uchida, M. Tomiha, H. Takizawa and M. Kawaraya, *J. Photochem. Photobiol., A*, 2004, **164**, 93–96.
26 Y. Kim, B. J. Yoo, R. Vittal, Y. Lee, N.-G. Park and K.-J. Kim, *J. Power Sources*, 2008, **175**, 914–919.
27 P. J. Holliman, M. L. Davies, A. Connell, B. Vaca Velasco and T. M. Watson, *Chem. Commun.*, 2010, **46**, 7256–7258.
28 P. R. F. Barnes, K. Miettunen, X. Li, A. Y. Anderson, T. Bessho, M. Grätzel and B. C. O'Regan, *Adv. Mater.*, 2013, **25**(13), 1881–922.
29 P. Joshi, L. Zhang, D. Davoux, Z. Zhu, D. Galipeau, H. Fong and Q. Qiao, *Energy Sci. Technol.*, 2010, **3**, 1507–1510.
30 M. Alkan, O. Demirbas and M. Dogan, *Fres. Env. Bull.*, 2004, **13**, 1112–1121.
31 J. Fan, W. Cai and J. Yu, *Chem.–Asian J.*, 2011, **6**, 2481–2490.
32 P. J. Holliman, B. Vaca Velasco, I. Butler, M. Wijdekop and D. A. Worsley, *Int. J. Photoenergy*, 2008, 1–8.
33 H. J. Snaith, *Energy Environ. Sci.*, 2012, **5**, 6513.
34 S. Ito, P. Chen, P. Comte, M. K. Nazeeruddin, P. Liska, P. Péchy and M. Grätzel, *Prog. Photovoltaics*, 2007, **15**, 603–612.
35 Y. Yamamoto, M. Kawaraya, H. Segawa, S. Uchida, J. Kano, F. Saito, K. Tsujimoto, T. Saito and S. Ito, *Chem. Lett.*, 2011, **40**, 1220–1222.
36 N. Park, J. van de Lagemaat and A. Frank, *J. Phys. Chem. B*, 2000, **104**, 8989–8994.
37 B. C. O'Regan, J. R. Durrant, P. M. Sommeling and N. J. Bakker, *J. Phys. Chem. C*, 2007, **111**, 14001–14010.
38 JCPDS 01-071-1168 (Anatase – TiO_2).
39 JCPDS 01-071-0650 (Rutile – TiO_2).
40 JCPDS 00-003-0888 (ZnO).
41 T. Baird, K. Campbell, P. J. Holliman, R. Hoyle, D. Stirling and D. P. Williams, *J. Chem. Soc., Faraday Trans.*, 1995, **91**, 3219–3230.